

Possible charge-density-wave signatures in the anomalous resistivity of Li-intercalated multilayer MoS₂

Erik Piatti,¹ Qihong Chen,² Mauro Tortello,¹ Jianting Ye,^{2,*} and Renato S. Gonnelli^{1,†}

¹*Department of Applied Science and Technology, Politecnico di Torino,
corso Duca degli Abruzzi 24, 10129 TO Torino, Italy*

²*Device Physics of Complex Materials, Zernike Institute for Advanced Materials,
Nijenborgh 4, 9747 AG Groningen, The Netherlands*

We fabricate ion-gated field-effect transistors (iFET) on mechanically exfoliated multilayer MoS₂. We encapsulate the flake by Al₂O₃, leaving the device channel exposed at the edges only. A stable Li⁺ intercalation in the MoS₂ lattice is induced by gating the samples with a Li-based polymeric electrolyte above ~ 330 K and the doping state is fixed by quenching the device to ~ 300 K. This intercalation process induces the emergence of anomalies in the temperature dependence of the sheet resistance and its first derivative, which are typically associated with structural/electronic/magnetic phase transitions. We suggest that these anomalies in the resistivity of MoS₂ can be naturally interpreted as the signature of a transition to a charge-density-wave phase induced by lithiation, in accordance with recent theoretical calculations.

Keywords: MoS₂ - Ionic gating - Intercalation - Anomalous resistance - Phase transitions - Charge density waves

I. INTRODUCTION

Interacting electrons in transition metal dichalcogenides (TMDs) have attracted a lot of attention, owing to the emergence of exotic electronic phases and the non-trivial physics that arise due to their competition [1]. Experimentally, these competing electronic phases are often the cause of anomalies in the temperature dependence of the electric transport - a characteristic feature of a wide variety of materials including oxides [2], arsenides [3], iron pnictides [4, 5], and metal chalcogenides [6, 7]. These anomalies mark the boundaries between different electronic phases, exhibiting transitions in the lattice, magnetic, electronic and topological degrees of freedom. Different transitions can also appear concurrently across the same boundary in a material's phase diagram. This can be incidental, if the two transitions are unrelated to one another [2]. Alternatively, their concomitant occurrence may result from a strong coupling between the underlying phases, when the transition in one degree of freedom triggers a transition in a second one [4, 5].

TMDs are layered compounds sharing the generalized MX₂ formula, where M is a transition metal (such as Mo, Nb, Ta, Ti, V, W) and X is a chalcogen (S, Se, Te) element [8, 9]. Different structural phases are possible in these materials depending on the coordination of the metal atom and the stacking of the individual layers, the most common being trigonal prismatic (2H), octahedral (1T) and distorted octahedral (1T') [8, 9]. For most - but not all - TMDs at room temperature, the 2H polytype is the most stable, while the other metastable polytypes can be obtained via alkali ion intercalation [8, 10].

TMDs feature complex electronic structures and complicated phase diagrams reminiscent of those of cuprates and iron pnictides [7], often dominated by the interplay between superconductivity (SC) and charge-density-wave (CDW) order [8]. CDWs are periodic modulations of the charge carrier density, associated to distortions of the underlying crystal lattice [11], which are often the result of strong electron-phonon coupling [12] and Fermi-surface nesting [13]. Their appearance and behavior in TMDs are strongly dependent on both the atomic components and the polytype [8]: although well known in several Nb-, Ta-, Ti-, and V-based TMDs [7], as well as metallic 1T'-MoTe₂ [14], this phenomenon has not been reported so far in the semiconducting phase of TMDs of the 2H polytype. Interestingly, however, the application of an external pressure in excess of ~ 10 GPa has been recently shown to induce a metallization of 2H-MoS₂, accompanied by the possible emergence of a CDW distortion [15].

At ambient pressure, the interplay between SC and CDWs in TMDs used to be accessed by carrier doping via intercalation [7, 16–20]. Recently, it was demonstrated that the same effect can be induced by the application of an electric field [21–23]. Structural transitions between different polytypes can also be controlled by electric field effect, as it has been shown in single-layer MoTe₂ between the 2H and 1T' phases - although the authors did not investigate whether this did also give rise to CDW order [24]. Indeed, carrier doping has been predicted to be able to induce different CDW phases in MoS₂ [25–27]. On the other hand, electrochemical intercalation holds great promise for tailoring its electric, optical and chemical properties, as well as making it very attractive in the field of energy storage for TMD-based alkali-ion batteries and supercapacitors [9]. In this sense, ionic gating can be an especially versatile tool for doping control. This technique incorporates an electrochemical cell in a top-gate transistor configuration, where the sample is separated from a gate counter-electrode by an electrolyte [28]. By

* j.ye@rug.nl

† renato.gonnelli@polito.it

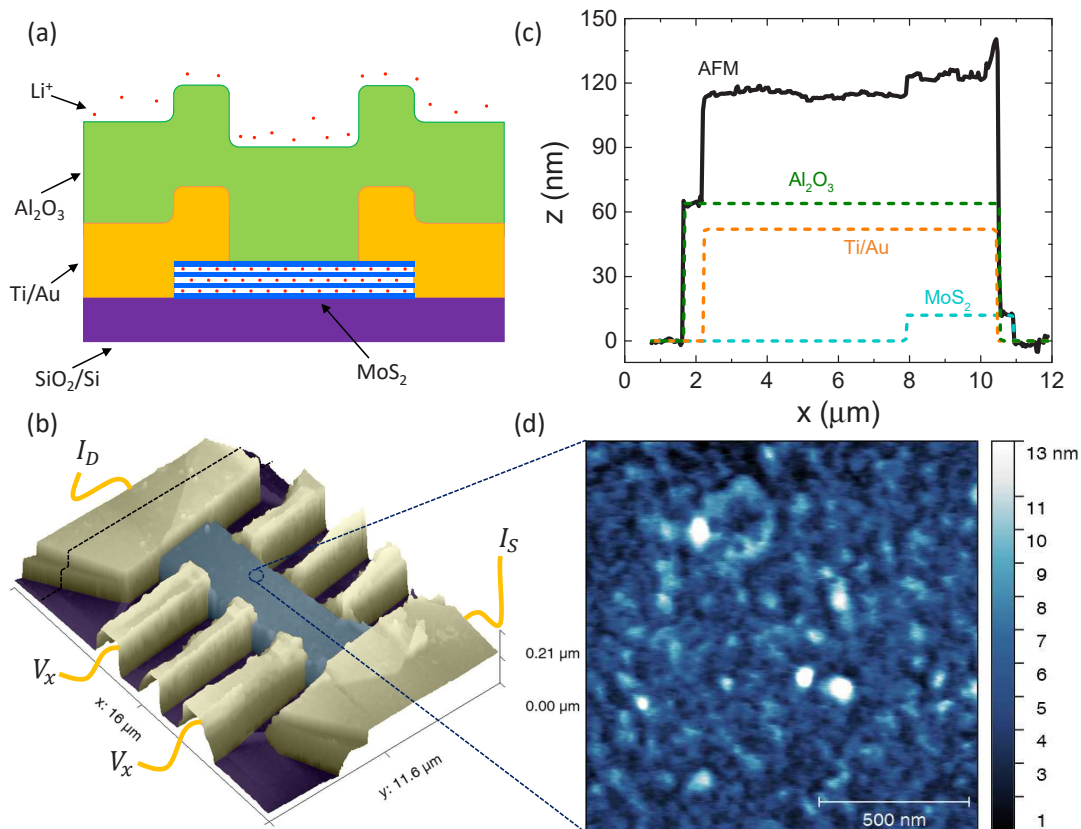


FIG. 1. (a) Sketch in side-view and (b) 3D rendering of the AFM topographic image in tapping mode of an Al_2O_3 -encapsulated few-layer MoS_2 device. Li^+ ions can directly access the MoS_2 flake only from the exposed sides of the device. V_G is applied between I_S and a coplanar side-gate electrode (not shown in the figure). (c) Height signal in correspondence to the black dashed line in (b) (black solid line). Dashed lines highlight the topographic contributions from the MoS_2 flake (blue), Ti/Au contacts (yellow) and Al_2O_3 encapsulation layer (green). (d) AFM topographic image in tapping mode of the same device in the area highlighted by the dashed blue circle in (b). Root mean square height is $S_q = 1.86$ nm, much smaller than the Al_2O_3 thickness (~ 60 nm).

properly selecting gating temperature and gate voltage, doping can be achieved either via electrostatic ion accumulation or bulk electrochemical intercalation. In the electrostatic regime, the gate voltage drives the ions to form an electric double layer at the surface of the sample, which acts as a nanoscale capacitor with a huge capacitance [22, 23, 29]. In the electrochemical regime, the strong interface electric field is exploited to drive the ions in the van der Waals gap between the layers, achieving gate-controlled intercalation [20, 29, 30].

In this work, we use ionic gating with a polymeric electrolyte to intercalate Li^+ ions in Al_2O_3 -encapsulated multilayer MoS_2 devices at high temperature. We find that the Li^+ -intercalated state is fully stable upon removal of the applied gate voltage, if the sample is quenched below the optimal intercalation temperature. No doping-induced SC state is observed down to ~ 3 K, but we find clear evidence for the emergence of sheet resistance (R_s) anomalies in the intercalated state around ~ 200 K. These anomalies evolve as a hump-dip struc-

ture in the first derivative, dR_s/dT . Upon increasing the gate voltage beyond the onset of intercalation, the hump feature strongly shifts to higher temperature, while the position of the dip feature remains mostly unaffected. We discuss how this behavior can be naturally linked with the appearance of the CDW phases predicted in Refs.[25–27] as a function of Li^+ doping. To the best of our knowledge, our results constitute the first report for non-Fermi liquid behavior in MoS_2 at ambient pressure.

II. RESULTS

A. Device fabrication

We first developed a procedure to fabricate encapsulated MoS_2 devices, where the only direct interface between the flakes and the electrolyte occurs at the sides of the flake (see Fig.1a). We obtained multilayer MoS_2 flakes by mechanical exfoliation [31] of $2H$ - MoS_2 bulk

crystals (SPI Supplies) on standard $\text{SiO}_2(300 \text{ nm})/\text{Si}$ substrates. Flakes with thicknesses around $\sim 10 \text{ nm}$ (number of layers ~ 15) were selected through their optical contrast [32], which were confirmed subsequently by atomic force microscopy (AFM). We chose this particular thickness to study the well-defined bulk properties [33], while minimizing the effect of lattice expansion in the z direction during the Li^+ intercalation, which can easily break the electrodes if the expansion is too severe in thicker samples. Electrical contacts to the flakes were patterned in Hall bar configuration by e-beam lithography, followed by evaporating $\text{Ti}(5 \text{ nm})/\text{Au}(50 \text{ nm})$ and lift-off. A large, interdigitated coplanar side-gate electrode was patterned $\sim 100 \mu\text{m}$ away from the flake [30]. Then, we deposited a $\text{Al}_2\text{O}_3(\sim 60 \text{ nm})$ mask over the electrodes and the rectangular channel of the Hall bar, leaving the irregular part of the flake exposed on all sides. Finally, we employed reactive ion etching (using Ar gas, RF Power: 100 W, etching duration: 2 min) to remove the exposed areas of the flake.

Fig.1b shows a 3D rendering of the AFM height signal acquired in tapping mode over a completed device before applying the electrolyte. We use false colors to clearly distinguish the different regions of the device (yellowish gray: leads, blue: channel, and violet: substrate). The Al_2O_3 encapsulation layer covers both the channel and the leads. Along the leads, it partially extends on the underlying substrate to provide complete insulation from the environment. On the device channel, it presents the sharp edge defined by RIE allowing direct exposure of the flake to the electrolyte only from the side. The stacking of the three materials, as sketched in Fig.1a, can be clearly recognized from the height profile of the AFM imaging (Fig.1c) along the black dashed line in Fig.1b. Height steps corresponding to the MoS_2 flake, the Ti/Au contacts and the Al_2O_3 encapsulation mask can be clearly recognized and are explicitly highlighted.

In Fig.1d, we present the surface topography of the channel region. The smooth Al_2O_3 encapsulation layer on atomically flat MoS_2 is free of pinholes or other defects that would allow penetration of ions from the electrolyte to the channel surface. Direct AFM profiling for a typical $1.5 \times 1.5 \mu\text{m}^2$ area shows that the root mean square roughness of the Al_2O_3 surface S_q equals 1.86 nm, which is more than 30 times smaller than the total oxide thickness.

For the intercalation experiments, we prepared the polymeric electrolyte by dissolving $\sim 25 \text{ wt.}\%$ of lithium bis(trifluoromethane)sulfonimide (Li-TFSI) in polyethylene glycol (PEG, $M_w \sim 450$) in an Ar-filled glove box. For the low-temperature control experiment (described in the following), we directly employed the ionic liquid 1-butyl-1-methylpiperidinium bis(trifluoromethylsulfonyl)imide (BMPPD-TFSI). Both electrolytes are liquid at room temperature, and the latter retains good ionic mobility down to $\sim 240 \text{ K}$. The electrolytes are pumped under vacuum at $\sim 330 \text{ K}$ for at least 1 hour before being drop casted on to the device,

covering both the channel and the Au side-gate electrode. Subsequently, the devices are quickly transferred to the cold plate of a Cryomech®PT405 pulse-tube cryocooler and allowed to degas under high vacuum ($\lesssim 10^{-5} \text{ mbar}$) for another 1 hour to minimize water absorption. This is necessary to eliminate the electrolysis of absorbed water, which might be activated easily before the expected intercalation due to the combination of high temperature and large applied gate voltage.

B. Electrochemical doping

We perform Li^+ intercalation in our encapsulated MoS_2 devices by applying gate voltage V_G ramps at high temperature ($T \gtrsim 330 \text{ K}$) and monitoring the sheet resistance R_s as a function of time. We employ the first channel of a two-channel Agilent B2912 Source-Measure Unit (SMU) to apply V_G and measuring the gate current I_G simultaneously. Then the R_s is determined in the four-wire configuration by applying a small constant DC current between the source and drain contacts of our devices ($I_{DS} \sim 1 \mu\text{A}$) with the second channel of the same SMU, and measuring the longitudinal voltage drop V_{xx} across two voltage contacts with an Agilent 34420 Nanovoltmeter. We remove the common mode errors, such as thermoelectric offsets and contributions from I_G , by averaging the R_s values acquired with the I_{DS} of opposite polarities (two-point delta mode).

As shown in Fig.2 a and b, the overall gating process can be divided into four main steps: doping, quenching, T -dependent characterization, and release. In the first step, the V_G is ramped following the profile shown in Fig. 2a at high $T = 330 \text{ K}$ and then kept constant for typically $\sim 15 \text{ min}$ allowing the insertion of ions into the flake. In the second step, the doping process is quenched by cooling the sample below the optimal intercalation temperatures while keeping the V_G constant. In the third step, the full temperature dependence of the R_s is investigated. This will be discussed in detail in the next section. In the fourth and final step, the V_G is ramped down to zero: depending on the T , at which this step is performed, the intercalated ions can be released back to the electrolyte, or remain confined in the MoS_2 lattice.

As shown in Figs.2b and 2c, for the modulation of the R_s as a function of V_G , the gating process can be separated into two regimes. For the low V_G , the modulation of R_s is mainly originated from driving the Li^+ ions by the applied electric field and accumulating them electrostatically onto the channel surface [29, 30]. For large values of V_G , the change in R_s is instead mainly caused by field-driven ion intercalation to the van der Waals gap between the MoS_2 layers [29, 30]. When the MoS_2 top surface is directly exposed to the electrolyte, it is difficult to separate the two regimes by considering only the behavior of R_s [30], therefore, additional information can be useful for clearer discrimination. Most notably the carrier density in the sample determined by Hall effect

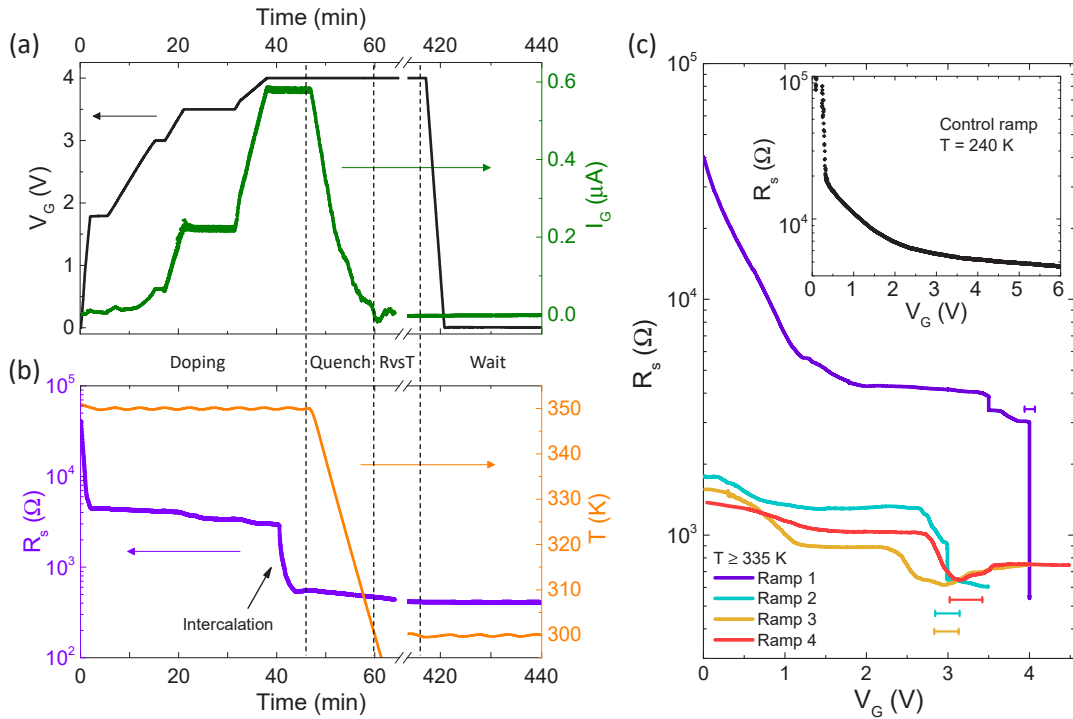


FIG. 2. Encapsulated MoS₂ doping dynamics. (a) V_G (black line, left axis) and I_G (green line, right axis) as a function of time during the doping process, quenching, characterization, and release. (b) R_s (violet line, left axis) and T (orange line, right axis) as a function of time. Dashed lines distinguish the different experimental steps. (c) R_s as a function of V_G for different V_G ramps. Ramp 1 is measured at $T \simeq 350$ K. Ramps 2,3,4 at $T \simeq 335$ K. All are performed using the PEG/Li-TFSI polymer electrolyte. Horizontal error bars indicate the uncertainty on the threshold voltage V_{th} for stable Li⁺ intercalation in each ramp. Inset shows a V_G ramp measured at $T \simeq 240$ K using pure BMPPD-TFSI ionic liquid for comparison.

[30] can be used as a useful guidance. On the other hand, when the top surface of the flake is protected by the Al₂O₃ layer, the encapsulation strongly suppresses the electrostatic gating on the device channel. Hence, the two regimes are clearly separated by the sharp R_s drop appearing when the ions penetrate between the layers [20].

Subsequently, the doping process is quenched by rapidly cooling down the sample. This procedure “locks” the intercalated ions in place and leads to a stable lithiation state for the MoS₂ flake. Indeed, once V_G is released to zero at a lower $T \sim 300$ K, no significant change in R_s can be detected on a time scale between tens of minutes to a few days. Note that, at this T , the electrolyte is still liquid and hence fully supports ion motion: thus, this behavior is qualitatively different from the “freezing” of the ions electrostatically accumulated in the form of the electric double layer when the system is cooled below the glass transition temperature of the electrolyte. The R_s increases again over time at $V_G = 0$ only when the sample is heated above $T \gtrsim 320$ K, signaling the onset of delithiation. Hence, lithiation-delithiation of the MoS₂ flake can be achieved above 320 K: after trial-and-error, we found out that gating at $T \sim 335$ K provided efficient doping while minimizing the chance of device failure at

high V_G .

In Fig.2c we show different V_G ramps, corresponding to different intercalation states. These are achieved by selecting different target V_G values while keeping the same doping time. However, the R_s drop clearly shows that, between successive ramps, the onset of intercalation does not remain unchanged, and is instead affected by the previous intercalation history of the flake. The different intercalation states can then more properly be mapped by how much the final applied V_G exceeds the onset of intercalation in that specific ramp, *i.e.* the “overdrive” voltage $V_G - V_{th}$, where V_{th} is the value of V_G where a stable Li⁺ incorporation is achieved. For ramps where R_s drops while V_G is not held constant, we choose V_{th} as the value of the minimum in the R_s vs. V_G curve. Hence, the electrostatic regime is identified by the condition $V_G - V_{th} < 0$, while the intercalation one by $V_G - V_{th} \gtrsim 0$.

Finally, we confirm that the R_s modulation at low V_G is due to electrostatic accumulation. To show this, we performed a control doping experiment using an ionic liquid and applied V_G at $T \sim 240$ K. It is well known that reducing the gating temperature strongly suppresses all electrochemical interactions maintaining pure electrostatic charging [28, 29, 34, 35]. Furthermore, due to much larger ions in the molecular ionic liquids, gate-driven in-

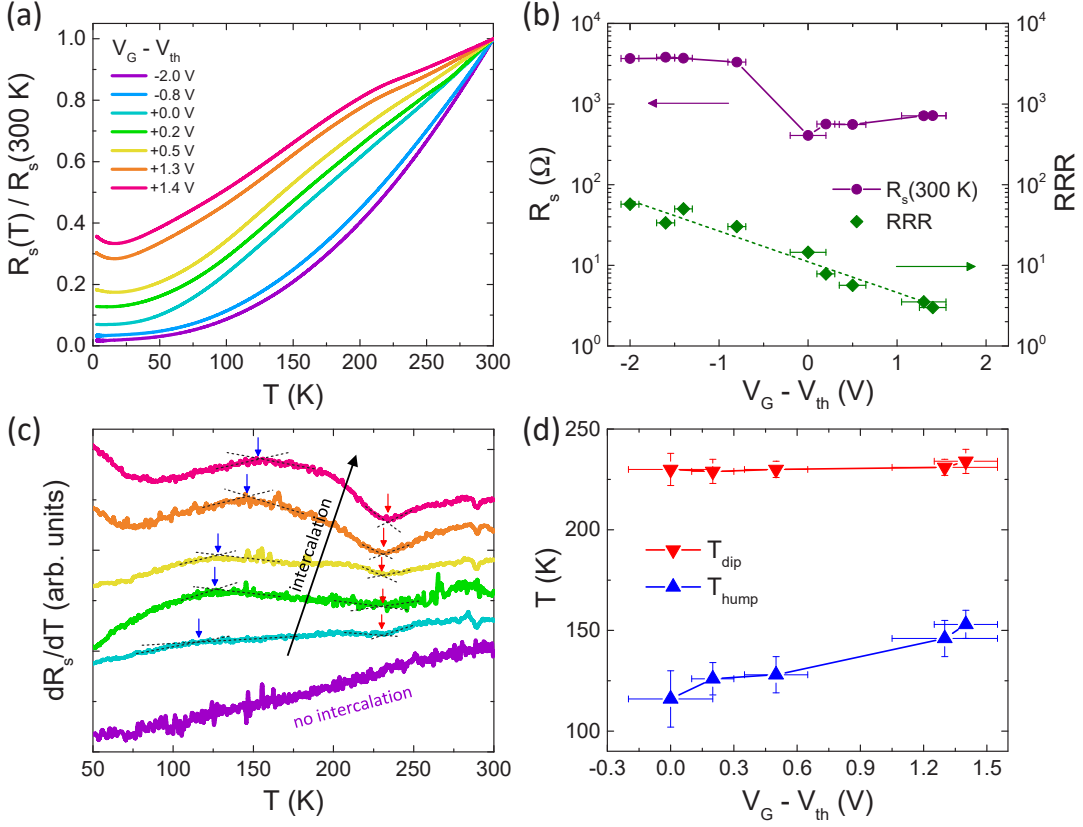


FIG. 3. Temperature dependence of the electrical transport. (a) R_s , normalized at $T = 300\text{ K}$, as a function of T , before and after the onset of Li^+ intercalation. (b) Overdrive voltage dependence of the R_s at $T = 300\text{ K}$ (violet dots and lines), and of the residual resistivity ratio (green diamonds). Dashed line acts as a guide to the eye. (c) T dependence of the first derivative of the R_s , before and after Li^+ intercalation. Curves are color-coded to match the legend in panel (a). Arrows indicate the T values where the first derivative shows a dip (red) and a peak (blue). Curves are shifted for clarity. (d) Overdrive voltage dependence of T_{hump} (blue up triangles) and T_{dip} (down red triangles) in (c).

tercalation of layered flakes by ionic liquids is known to result in immediate device failure due to delamination and destruction of the crystal structure [20]. As we show in the inset to Fig.2c, gating an encapsulated device with pure BMPPD-TFSI ionic liquid results in a featureless, monotonically decreasing dependence of R_s on V_G , and a comparable R_s modulation with respect to the $V_G - V_{th} < 0$ regime of Li-TFSI gating at $T \gtrsim 330\text{ K}$. In both cases the flakes quickly revert to their native insulating states by simply removing V_G , further supporting the electrostatic picture. Note that an Al_2O_3 layer with a thickness $d \sim 60\text{ nm}$ ($\epsilon_r \sim 9$ [36]) provides a residual, non-negligible top-gate capacitance $C_{ox} = \epsilon_r \epsilon_0 / d \sim 130\text{ nF/cm}^2$, where ϵ_0 is the vacuum permittivity. It is worth noting that an additional electrostatic contribution may also arise from quasi-1D channels induced at the exposed sides of the MoS_2 flakes.

We now show the electric transport of our encapsulated devices down to $T \sim 3\text{ K}$, both before ($V_G - V_{th} < 0$) and after ($V_G - V_{th} \gtrsim 0$), the onset of intercalation. Fig.3a shows the T -dependence of the resistance, normalized by

its value at 300 K . The samples show clear metallic behavior both in the electrostatic and intercalated regimes. In Fig.3b we plot two figures of merit for the transport properties as a function of $V_G - V_{th}$: the sheet resistance at 300 K , $R_s(300\text{ K})$, and the residual resistivity ratio RRR defined as $R_s(300\text{ K})/R_{s,0}$, where $R_{s,0}$ is the minimum of R_s over the entire measured T range. The behavior of $R_s(300\text{ K})$ well reproduces our observation that, during the doping process, encapsulating the flake with Al_2O_3 is crucial to clearly distinguish surface and bulk-doped states as shown by the sharp drop in R_s close to V_{th} . The decreasing dependence of RRR instead indicates that carrier mobility is strongly suppressed by increasing V_G , especially in the intercalation regime. This behavior is possibly affected by the randomness caused by intercalation and progressive introduction of extra scattering centers due to the presence of the ions themselves, irrespectively of the material under study [30, 37–40].

For $V_G - V_{th} < 0$, R_s is a smooth increasing function of T . The large RRR values in this regime indicate that defects provide a small contribution to the total car-

rier scattering rate at high T . This can be associated to the insulation of the device from the ionic environment provided by the encapsulation layer, and is consistent with the drastically enhanced carrier mobility reported in MoS₂ transistors encapsulated with Al₂O₃ [41] and other high- κ dielectrics [42]. For $V_G - V_{th} \geq 0$, however, a clear change of slope appears in the temperature dependence of R_s around ~ 200 K. This anomalous ‘‘hump’’ becomes more evident for larger values of $V_G - V_{th}$. Below this hump ($T \lesssim 200$ K), the R_s drops more rapidly with the decrease of T . At the same time, we observe the emergence of a resistance upturn for $T \lesssim 20$ K. This indicates that, at low T and high doping, metallic behavior is suppressed.

The behavior of the resistance hump around ~ 200 K can be best visualized by the T dependence of the first derivative of R_s , dR_s/dT , both before and after intercalation as shown in Fig.3c. When the sample is not intercalated (violet curve), dR_s/dT is a featureless function of T . In the intercalated state (upon increasing doping: light blue, green, yellow, orange and red curves), the resistance anomaly gives rise to a clear dip-hump structure in the T dependence of dR_s/dT : a sharp dip at higher T (T_{dip} , highlighted by the red arrows), and a broader hump at lower T (T_{hump} , blue arrows). These two features evolve differently with increasing doping: as we show in Fig.3d, the T_{hump} strongly increases with increasing $V_G - V_{th}$, while the T_{dip} is nearly constant.

III. DISCUSSION

Resistance anomalies in TMDs are usually associated with phase transitions to various CDW phases [7]. These are ubiquitous in Nb-, Ta- and Ti-based dichalcogenides for both main polytypes (trigonal prismatic $2H$ and octahedral $1T$) [7], with the exception of NbS₂ [43]. In particular, CDW transitions are observed in the T dependence of the resistivity of undoped TMDs as large, hysteretic jumps in insulating compounds [21, 44, 45], and as less apparent humps in metallic ones [43, 46, 47].

Experimentally, doping can control CDW phases in TMDs, both by field-effect carrier accumulation at the surface [21–23] as well as ion intercalation in the bulk [16, 17, 19, 20, 48]. Generally, increase of carrier doping causes strong suppression of the CDW phases, favoring the onset of SC order [16, 17, 19–22, 48]. This, however, is not true for all compounds: for example, it has recently been demonstrated that doping strengthens the CDW phase both in $2H$ -NbSe₂ and $2H$ -TaSe₂ thin flakes [23].

We thus consider whether the resistance anomalies we observed in encapsulated Li_xMoS₂ could be attributed to the emergence of a CDW phase. Such an interpretation would naturally account for the two different features observed in dR_s/dT at T_{hump} and T_{dip} , as well as their doping dependence. Indeed, in other TMDs, the dip in dR_s/dT is associated to a transition to an incommensurate CDW phase at higher T , which is weakly de-

pendent on doping [19], while the peak in dR_s/dT to the further transition to a commensurate CDW phase at lower T , with a strong doping dependence [19]. In addition, Ref.[25] predicted that sufficiently strong electron doping ($\gtrsim 0.15$ e⁻/cell) would also cause the suppression of the SC dome in $2H$ -MoS₂, and the appearance of CDW order due to phonon instabilities. Conversely, Ref.[26] calculated that both electron and hole doping may trigger a structural phase transition in MoS₂, from the semiconducting $2H$ phase to the metallic $1T$ phase. Furthermore, they predicted that while hole doping stabilizes the metastable $1T$ phase, electron doping would then promote the transition to the more stable, distorted $1T'$ phase. The latter can be regarded as a CDW restructuring of the metallic $1T$ phase and should exhibit semimetallic behavior with a graphene-like Dirac cone in absence of spin-orbit coupling [26].

Strictly speaking, these theoretical results were calculated for a single-layer. Nevertheless, we expect multi-layer samples to follow a qualitatively similar behavior, since bulk lithiation has been explicitly predicted to promote CDW transitions in both the $2H$ and $1T$ polytypes [27]. Notably, CDW order is expected to be weaker in the $2H$ structure, with moderate lattice distortion and suppressed electron localization, while the opening of a full band gap is predicted for the $1T$ structure [27]. Indeed, the TMD phase engineering by lithium intercalation has explicitly been demonstrated [49]: in the case of MoS₂, lithiation of the pristine $2H$ structure can result in the formation of both the regular $1T$ and distorted $1T'$ structures, as observed in STEM and Raman measurements [50, 51]. A similar behavior was observed in Re-doped MoS₂ as well [52].

A further consistency check between the behavior of our samples and the onset of a CDW phase can be obtained by assessing the scaling of the T dependence of the R_s in the intercalated state. In $2H$ -NbSe₂, TaS₂ and TaSe₂, the CDW ordering is phenomenologically associated with a pronounced change in the slope of the T dependence of $R(T)$, when plotted in log-log scale. At high T , the scaling is linear in T due to large-angle carrier scattering by acoustic phonons [43]. At low T , the scattering follows a T^p dependence due to small-angle electron-phonon scattering instead [43]. The value of p depends on the orbital symmetry of the bands involved in the scattering process: scattering from s -like bands, such as in $2H$ -TaS₂ and TaSe₂, gives $p = 5$ [43], while scattering from d -like bands, such as in $2H$ -NbSe₂, gives $p = 3$ [43]. Larger values of p are also considered as a measure of stronger CDW strength [43]. For the T between these extremes, scaling with an intermediate $p \simeq 2$ is expected corresponding to the scattering by CDW fluctuations [43].

As shown in Fig.4, for $T \gtrsim 200$ K, our devices show a T^p scaling with p between 1 and 1.5. This reproduces well the behavior in bulk intercalated samples described in literature [53] (black dots in Fig.4). The slightly super-linear scaling can be originated from both doping in-

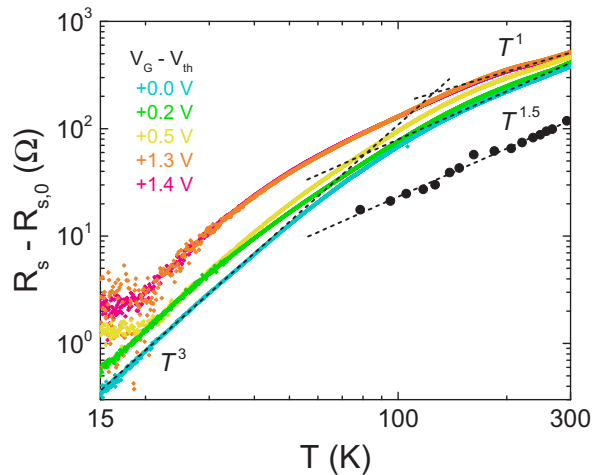


FIG. 4. Double logarithmic plot of the increase of R_s in the range 15 – 300 K for Li^+ -intercalated MoS_2 (small diamonds) and $\text{K}_{0.4}\text{MoS}_2$ (black dots) from Ref.53. Dashed lines that represent the T^1 , $T^{1.5}$, and T^3 power-law dependences are shown for comparison.

homogeneity [53] and additional scattering with optical phonons [54]. For $T \lesssim 40$ K, and neglecting the localization upturn close to the lowest T , the curves present a scaling very close to $p = 3$. This is consistent with the dominant orbital d -character of the conduction band of MoS_2 [55]. Intermediate values of T show a further scaling behavior with $p \simeq 1.6$ to 2.1.

As substantiated by the discussion above, our results are consistent with a doping-induced CDW ordering in Li_xMoS_2 . However, transport measurements alone cannot distinguish between different possible scenarios leading to such a behavior. In the simplest scenario, that is proposed in Ref.[25], Li^+ ions simply provide charge carriers to the system, which undergoes a CDW transition by a reconstruction of the $2H$ structure (similarly to what was observed under external pressure [15]). This would place the CDW phase in competition with SC order present at lower doping. We point out that no sample that presented the R_s anomalies showed any kind of SC transition. This is in contrast to our earlier report [30], where Li_xMoS_2 flakes showed SC at $T \lesssim 3.7$ K while not showing R_s anomalies at higher T . There are two main differences between these experiments. On one hand, in the present work the flakes are encapsulated, which eliminates the possibility of inducing superconductivity by field effect. Indeed, encapsulation has been shown to promote CDW ordering in TMDs [56]. More importantly, the devices in Ref.[30] were intercalated at a lower $T = 300$ K, thus strongly suppressing ionic mobility in the flake. Thus, the devices presented in this work may all show larger doping levels even at $V_G - V_{th} \simeq 0$, placing their state well beyond the peak of SC dome, and pushing T_c well below the lowest T accessible in our experiment (3 K).

Another possibility is that the larger intercalation $T \gtrsim 330$ K employed in this work allowed for a structural phase transition away from the pristine $2H$ polytype [26, 27]. Thus, a second scenario would more closely follow the picture proposed in Ref.[26]. Doping with Li^+ ions would first induce a structural transition of the MoS_2 from the $2H$ to the $1T$ phase. Then the metastable $1T$ phase would undergo a CDW transition into the distorted $1T'$ phase at lower temperatures. Alternatively, doping could also induce a transition directly from the $2H$ to the $1T'$ phase, as theoretically suggested in Ref.[10]. In this case, the observed transport anomalies would require the presence of multiple CDW distortions available for the system, which have been predicted for $1T'$ - MoTe_2 [57]. Finally, we cannot rule out the possibility that the sample remains in the $2H$ phase at high T and undergoes a purely structural transition to the $1T/1T'$ phases during the cool down. However, we deem this last possibility unlikely due to the metastable nature of the $1T$ phase and the energy barrier that separates the two polytypes even in presence of Li^+ intercalants [26], which would hinder a transition at lower temperatures. These points cannot be settled purely by electric transport measurements, and further work will require using structure-sensitive techniques to characterize Li_xMoS_2 both as a function of T and doping, such as Raman spectroscopy or X-ray diffraction studies.

IV. CONCLUSIONS

In summary, we fabricated multilayer MoS_2 devices to investigate the effects of field-driven Li^+ intercalation with a polymeric electrolyte at $T \gtrsim 330$ K. To minimize the influence of ion accumulation at the surface, we encapsulated our devices with Al_2O_3 high- κ dielectric, and employed RIE to obtain well-defined device geometry and edges, leaving only the sides of the flake exposed to the electrolyte. The resulting device architecture was confirmed via AFM. We monitored the effects of field-driven Li^+ intercalation by measuring R_s in our devices as a function of V_G and T . Encapsulation allowed us to clearly distinguish between surface ion accumulation and bulk ion intercalation by the presence of sharp drops in the R_s vs. V_G and time curves. We confirmed the electrostatic operation of our devices before the onset of intercalation by gating with a pure ionic liquid at $T \sim 240$ K. The doping process at high T resulted in stable Li^+ incorporation in the MoS_2 lattice even when the electrolyte was still liquid, as long as the sample was then quenched below 320 K. We characterized the T dependence of R_s in the intercalated samples down to ~ 3 K, and observed anomalous metallic transport with a doping-induced hump in R_s around $T \sim 200$ K. These anomalous features strongly suggest the onset of a possible phase transition in the intercalated flakes, and are the first report of anomalous metallic character in MoS_2 at ambient pressure. In analogy with the behavior of

several other TMDs, and in accordance with theoretical predictions from the literature, we propose an interpretation of these anomalies in terms of the formation of a CDW phase at large Li^+ doping.

ACKNOWLEDGMENTS

Q. Chen and J. T. Ye acknowledge funding from the European Research Council (Consolidator Grant No. 648855 Ig-QPD).

-
- [1] A. L. Efros, M. Pollak, *Electron-electron interactions in disordered systems*, 1st Edition, Vol. 10, Elsevier, North Holland, 1985.
- [2] A. J. Campbell, G. Balakrishnan, M. R. Lees, D. M. Paul, G. J. McIntyre, Single-crystal neutron-diffraction study of a structural phase transition induced by a magnetic field in $\text{La}_{1-x}\text{Sr}_x\text{MnO}_3$, *Phys. Rev. B* 55 (1997) R8622(R).
- [3] A. Beleanu, et al., Large resistivity change and phase transition in the antiferromagnetic semiconductors LiMnAs and LaOMnAs , *Phys. Rev. B* 88 (2013) 184429.
- [4] S.-H. Baek, N. J. Curro, T. Klimczuk, E. D. Bauer, F. Ronning, J. D. Thompson, First-order magnetic transition in single-crystalline CaFe_2As_2 detected by ^{75}As nuclear magnetic resonance, *Phys. Rev. B* 79 (2009) 052504.
- [5] J. J. Wu, J. F. Lin, X. C. Wang, Q. Q. Liu, J. L. Zhu, Y. M. Xiao, P. Chow, C. Q. Jin, Magnetic and structural transitions of SrFe_2As_2 at high pressure and low temperature, *Sci. Rep.* 4 (2014) 3685.
- [6] S. Katayama, Anomalous resistivity in structural phase transition of IV–VI, *Solid State Commun.* 19 (1976) 381.
- [7] R. A. Klemm, Pristine and intercalated transition metal dichalcogenide superconductors, *Physica C* 514 (2015) 86.
- [8] S. Manzeli, D. Ovchinnikov, D. Pasquier, O. V. Yazyev, A. Kis, 2D transition metal dichalcogenides, *Nat. Rev. Mater.* 2 (2017) 17033.
- [9] W. Choi, N. Choudhary, G. H. Han, J. Park, D. Akinwande, Y. H. Lee, Recent development of two-dimensional transition metal dichalcogenides and their applications, *Mater. Today* 20 (2017) 116.
- [10] A. N. Enyashin, G. Seifert, Density-functional study of Li_xMoS_2 intercalates ($0 \geq x \geq 1$), *Comput. Theor. Chem.* 999 (2012) 13.
- [11] L. P. Gor'kov, G. Grüner, *Charge Density Waves In Solids*, 1st Edition, Vol. 25, Elsevier, North Holland, 1989.
- [12] K. Rossnagel, On the origin of charge-density waves in select layered transition-metal dichalcogenides, *J. Phys. Condens. Matter* 23 (2011) 213001.
- [13] X. Zhu, Y. Cao, J. Zhang, E. W. Plummer, J. Guo, Classification of charge density waves based on their nature, *Proc. Natl. Acad. Sci. USA* 112 (2015) 2367.
- [14] D. H. Keum, et al., Bandgap opening in few-layered monoclinic MoTe_2 , *Nat. Phys.* 11 (2015) 482.
- [15] Z.-Y. Cao, J.-W. Hu, A. F. Goncharov, Z.-J. Chen, Nontrivial metallic state of molybdenum disulfide, arXiv:1801.06351.
- [16] L. Fang, Y. Wang, P. Y. Zou, L. Tang, Z. Xu, H. Chen, C. Dong, L. Shan, H. H. Wen, Fabrication and superconductivity of Na_xTaS_2 crystals, *Phys. Rev. B* 72 (2005) 014534.
- [17] E. Morosan, H. W. Zandbergen, B. S. Dennis, J. W. G. Bos, Y. Onose, T. Klimczuk, A. P. Ramirez, N. P. Ong, R. J. Cava, Superconductivity in Cu_xTiSe_2 , *Nat. Phys.* 2 (2006) 544.
- [18] K. E. Wagner, et al., Tuning the charge density wave and superconductivity in Cu_xTaS_2 , *Phys. Rev. B* 78 (2009) 104520.
- [19] D. Bhoi, S. Khim, W. Nam, B. S. Lee, C. Kim, B.-G. Jeon, B. H. Min, S. Park, K. H. Kim, Interplay of charge density wave and multiband superconductivity in $2\text{H-Pd}_x\text{TaSe}_2$, *Sci. Rep.* 6 (2016) 24068.
- [20] Y. Yu, F. Yang, X. F. Lu, Y. J. Yan, Y. H. Cho, L. Ma, X. Niu, S. Kim, Y.-W. Son, D. Feng, S. Li, S.-W. Cheong, X. H. Chen, Y. Zhang, Gate-tunable phase transitions in thin flakes of 1T-TaS_2 , *Nat. Nanotechnol.* 10 (2015) 270.
- [21] M. Yoshida, Y. Zhang, J. T. Ye, R. Suzuki, Y. Imai, S. Kimura, A. Fujiwara, Y. Iwasa, Controlling charge-density-wave states in nano-thick crystals of 1T-TaS_2 , *Sci. Rep.* 4 (2015) 7302.
- [22] L. J. Li, E. C. T. O'Farrel, K. P. Loh, G. Eda, B. Özyilmaz, A. H. C. Neto, Controlling many-body states by the electric-field effect in a two-dimensional material, *Nature* 529 (2016) 185.
- [23] X. X. Xi, H. Berger, L. Forró, J. Shan, K. F. Mak, Gate tuning of electronic phase transitions in two-dimensional NbSe_2 , *Phys. Rev. Lett.* 117 (2016) 106801.
- [24] Y. Wang, et al., Structural phase transition in monolayer MoTe_2 driven by electrostatic doping, *Nature* 550 (2016) 487.
- [25] M. Rösner, S. Haas, T. O. Wehling, Phase diagram of electron-doped dichalcogenides, *Phys. Rev. B* 90 (2014) 245105.
- [26] H. L. Zhuang, M. D. Johannes, A. K. Singh, R. G. Hennig, Doping-controlled phase transitions in single-layer MoS_2 , *Phys. Rev. B* 96 (2017) 165305.
- [27] X. B. Chen, Z. L. Chen, J. Li, Critical electronic structures controlling phase transitions induced by lithium ion intercalation in molybdenum disulphide, *Chin. Sci. Bull.* 58 (2013) 1632.
- [28] K. Ueno, H. Shimotani, H. T. Yuan, J. T. Ye, M. Kawasaki, Y. Iwasa, Field-induced superconductivity in electric double layer transistors, *J. Phys. Soc. Jpn.* 83 (2014) 032001.
- [29] W. Shi, J. T. Ye, Y. Zhang, R. Suzuki, M. Yoshida, J. Miyazaki, N. Inoue, Y. Saito, Y. Iwasa, Superconductivity series in transition metal dichalcogenides by ionic gating, *Sci. Rep.* 5 (2015) 12534.
- [30] E. Piatti, Q. Chen, J. T. Ye, Strong dopant dependence of electric transport in ion-gated few-layer MoS_2 , *Appl. Phys. Lett.* 111 (2017) 013106.
- [31] K. S. Novoselov, D. Jiang, F. Schedin, T. J. Booth, V. V. Khotkevich, S. V. Morozov, A. K. Geim, Two-dimensional atomic crystals, *Proc. Natl. Acad. Sci. USA* 102 (2005) 10541.
- [32] H. Li, J. Wu, X. Huang, G. Lu, J. Yang, X. Lu, Q. Xiong, H. Zhang, Phase restructuring in transition

- metal dichalcogenides for highly stable energy storage, *ACS Nano* 7 (2013) 10344.
- [33] A. Splendiani, L. Sun, Y. B. Zhang, T. S. Li, J. Kim, C. Y. Chim, G. Galli, F. Wang, Emerging photoluminescence in monolayer MoS₂, *Nano Lett.* 10 (2010) 1271.
- [34] J. T. Ye, Y. J. Zhang, R. Akashi, M. S. Bahramy, R. Arita, Y. Iwasa, Superconducting dome in a gated band insulator, *Science* 338 (2012) 1193.
- [35] E. Piatti, D. De Fazio, D. Daghero, S. R. Tamalampudi, D. Yoon, A. C. Ferrari, R. S. Gonnelli, Multivalley superconductivity in ion-gated MoS₂ layers, arXiv:1802.06675.
- [36] M. J. Biercuk, D. J. Monsma, C. M. Marcus, J. S. Becker, R. G. Gordon, Low-temperature atomic-layer-deposition lift-off method for microelectronic and nanoelectronic applications, *Appl. Phys. Lett.* 84 (2003) 2405.
- [37] P. Gallagher, M. Y. Lee, T. A. Petach, S. W. Stanwyck, J. R. Williams, K. Watanabe, T. Taniguchi, D. Goldhaber-Gordon, A high-mobility electronic system at an electrolyte-gated oxide surface, *Nat. Commun.* 6 (2015) 6437.
- [38] D. Ovchinnikov, F. Gargiulo, A. Allain, D. J. Pasquier, D. Dumcenco, C. H. Ho, O. V. Yazyev, A. Kis, Disorder engineering and conductivity dome in ReS₂ with electrolyte gating, *Nat. Commun.* 7 (2016) 12391.
- [39] E. Piatti, S. Galasso, M. Tortello, J. R. Nair, C. Gerbaldi, M. Bruna, S. Borini, D. Daghero, R. S. Gonnelli, Carrier mobility and scattering lifetimes in electric-double-layer gated few-layer graphene, *Appl. Surf. Sci.* 395 (2017) 37.
- [40] R. S. Gonnelli, E. Piatti, A. Sola, M. Tortello, F. Dolcini, S. Galasso, J. R. Nair, C. Gerbaldi, E. Cappelluti, M. Bruna, A. C. Ferrari, Weak localization in electric-double-layer gated few-layer graphene, *2D Mater.* 4 (2017) 035006.
- [41] S. Y. Kim, S. Park, W. Choi, Enhanced carrier mobility of multilayer MoS₂ thin-film transistors by Al₂O₃ encapsulation, *Appl. Phys. Lett.* 109 (2016) 152101.
- [42] D. Kufer, G. Konstantatos, Highly sensitive, encapsulated MoS₂ photodetector with gate controllable gain and speed, *Nano Lett.* 15 (2015) 7307.
- [43] M. Naito, S. Tanaka, Electrical transport properties in 2H-NbS₂, -NbSe₂, -TaS₂ and -TaSe₂, *J. Phys. Soc. Jpn.* 51 (1982) 219.
- [44] J. A. Wilson, F. J. DiSalvo, S. Mahajan, Charge-density waves and superlattices in the metallic layered transition metal dichalcogenides, *Adv. Phys.* 24 (1975) 117.
- [45] B. Sipoš, A. F. Kusmartseva, A. Akrap, H. Berger, L. Forró, E. Tutiš, From mott state to superconductivity in 1T-TaS₂, *Nat. Mater.* 7 (2008) 960.
- [46] J. P. Tidman, O. Singh, A. E. Curzon, R. F. Frindt, The phase transition in 2H-TaS₂ at 75 k, *Phil. Mag.* 30 (1974) 1191.
- [47] X. Xi, L. Zhao, Z. Wang, H. Berger, L. Forró, J. Shan, K. F. Mak, Strongly enhanced charge-density-wave order in monolayer NbSe₂, *Nat. Nanotechnol.* 15 (2015) 765.
- [48] X. Zhu, et al., Anisotropic intermediate coupling superconductivity in Cu_{0.03}TaS₂, *J. Phys. Condens. Matter* 21 (2009) 145701.
- [49] D. Voiry, A. Mohite, M. Chhowalla, Phase engineering of transition metal dichalcogenides, *Chem. Soc. Rev.* 44 (2015) 2702.
- [50] G. Eda, T. Fujita, H. Yamaguchi, D. Voiry, M. Chen, M. Chhowalla, Coherent atomic and electronic heterostructures of single-layer MoS₂, *Nano Lett.* 6 (2012) 7311.
- [51] K. Leng, Z. Chen, X. Zhao, W. Tang, B. Tian, C. T. Nai, W. Zhou, K. P. Loh, Phase restructuring in transition metal dichalcogenides for highly stable energy storage, *ACS Nano* 10 (2016) 9208.
- [52] Y.-C. Lin, D. O. Dumcenco, Y.-S. Huang, K. Suenaga, Atomic mechanism of the semiconducting-to-metallic phase transition in single-layered MoS₂, *Nat. Nanotechnol.* 9 (2014) 391.
- [53] A. M. Hermann, R. Somoano, V. Hadek, A. Rembaum, Electrical resistivity of intercalated molybdenum disulfide, *Solid State Commun.* 13 (1973) 1065.
- [54] Z. Yu, Z.-Y. Ong, S. Li, J.-B. Xu, G. Zhang, Y.-W. Zhang, Y. Shi, X. Wang, Analyzing the carrier mobility in transition-metal dichalcogenide MoS₂ field-effect transistors, *Adv. Funct. Mater.* 27 (2017) 1604093.
- [55] G.-B. Liu, W.-Y. Shan, Y. Yao, W. Yao, D. Xiao, Three-band tight-binding model for monolayers of group-vib transition metal dichalcogenides, *Phys. Rev. B* 88 (2013) 085433.
- [56] S. Yan, W. Qiao, X. He, X. Guo, L. Xi, W. Zhong, Y. Du, Enhancement of magnetism by structural phase transition in MoS₂, *Appl. Phys. Lett.* 106 (2015) 012408.
- [57] J.-H. Lee, Y.-W. Son, Reentrant quantum spin hall states in charge density wave phase of doped single-layer transition metal dichalcogenides, arXiv:1711.08073v1.